

High-speed characteristics of vertical cavity surface emitting lasers and resonant-cavity-enhanced photodetectors based on intracavity-contacted structure

Y. M. Song,¹ B. K. Jeong,¹ B. H. Na,¹ K. S. Chang,² J. S. Yu,³ and Y. T. Lee^{1,*}

¹Department of Information and Communications, Gwangju Institute of Science and Technology, Gwangju 500-712, South Korea

²Division of Instrument Development, Korea Basic Science Institute, Daejeon 305-333, South Korea

³Department of Electronic Engineering, Kyung Hee University, Yongin 446-701, South Korea

*Corresponding author: ytleee@gist.ac.kr

Received 2 February 2009; revised 1 May 2009; accepted 8 May 2009;
posted 11 May 2009 (Doc. ID 106095); published 29 May 2009

We fabricated vertical cavity surface emitting lasers (VCSELs) and resonant-cavity-enhanced photodetectors (RCE-PDs) with GaAs/AlGaAs distributed Bragg reflectors (DBRs), operating at $\lambda \sim 980$ nm, based on an intracavity-contacted structure. The top-DBR mesa diameter of the VCSELs was optimized to $18\ \mu\text{m}$ in terms of slope efficiency, differential series resistance, and 3 dB bandwidth. For VCSELs with an oxide aperture of $4.5\ \mu\text{m}$ and a top-DBR mesa diameter of $18\ \mu\text{m}$, the threshold current was about 1.2 mA, exhibiting maximum output power of ~ 3.49 mW (at 20°C) with good uniformity. The effect of the overetching in the outermost layer of RCE-PDs on the device performance was also investigated. For RCE-PDs based on the VCSEL structure, a peak responsivity of $0.44\ \text{A/W}$ (at $\lambda \sim 979.7$ nm) with a spectral width of ~ 3 nm and a dark current of 68 pA under a bias voltage of -5 V at 20°C was obtained. The maximum 3 dB bandwidths of ~ 11.5 GHz with a modulation current efficiency factor of $5.6\ \text{GHz}/\text{mA}^{1/2}$ at -7 mA and 9 GHz at -7 V were achieved for VCSELs and RCE-PDs, respectively. © 2009 Optical Society of America

OCIS codes: 140.7260, 040.5160, 200.4650.

1. Introduction

Optical interconnects, which can remove bottlenecks (i.e., speed, packaging, fan-out, power dissipation) in electronic interconnects, have great potential for a next-generation computing platform and data links because of large bandwidth, high data throughput, and low power consumption, less sensitivity to electromagnetic interference, and low crosstalk noise [1,2]. The optical interconnection technique has been

developed either in hybrid or in monolithic form of device integration [3–5]. So far, hybrid integration of optoelectronic devices with the silicon integrated circuits (ICs), including driver/receiver ICs, is the most viable technique due to the low emission efficiency of Si photonics [3,5]. The crucial issue is the reduction of package cost, but functionality such as bidirectional data transmission schemes is also important to progress towards efficient optical interconnects. System requirements in optical interconnects are small-size high-speed optoelectronic devices such as light sources and photodetectors (PDs), allowing for multichannel parallel interconnections.

Vertical-cavity surface-emitting lasers (VCSELs) have emerged as a promising candidate for the light source of short-reach parallel optical data links due to their excellent performance (e.g., high-speed modulation, narrow beam divergence, high-volume production, and low cost), allowing them to be fabricated in two-dimensional arrays [6,7]. On the other hand, the resonant-cavity-enhanced (RCE)-PDs based on VCSEL structures have attracted considerable interest because of their potential for high quantum efficiency and high speed. Thus, the monolithic integration of VCSELs and RCE-PDs can be a cost-effective choice as a light source–photodetector combination for bidirectional chip-to-chip optical interconnects [8]. Most of VCSELs and RCE-PDs have employed extracavity-contacted structures [9–12]. Although high speed operation of extracavity-contacted VCSELs has recently been reported, the intracavity-contacted scheme has several advantages compared to the extracavity-contacted scheme. The co-planar metal contacts in an intracavity-contacted structure reduce parasitic capacitance [13,14]. Furthermore, lower optical losses in both un-

doped distributed Bragg reflector (DBR) mirrors provide higher quantum efficiency in both VCSELs and RCE-PDs. In this paper, we report the fabrication and characterization of 980 nm InGaAs/GaAs oxide-aperture VCSELs and RCE-PDs with intracavity-contacted structures from the same epitaxial wafer, exhibiting a high-speed operation of approximately 10 GHz.

2. Device Fabrication

Figure 1 shows schematic illustrations of (a) intracavity-contacted VCSELs with oxide aperture and (b) intracavity-contacted RCE-PDs from the same epitaxial wafer. All epitaxial layers were grown on semi-insulating (100) GaAs substrates by molecular beam epitaxy (DCA P600). The active region consists of three 85 Å-thick $\text{In}_{0.19}\text{Ga}_{0.81}\text{As}$ wells with 100 Å-thick GaAs barriers, surrounded by 1061 Å $\text{Al}_{0.32}\text{Ga}_{0.68}\text{As}$ cladding layers to form a 1λ-thick cavity. The cavity is bounded on each side by $\text{Al}_{0.98}\text{Ga}_{0.02}\text{As}$ oxidation layers, followed by *p*- and *n*-doped $5\lambda/4$ -thick GaAs contact layers. The bottom and top DBR mirrors (without doping) consist of 30.5

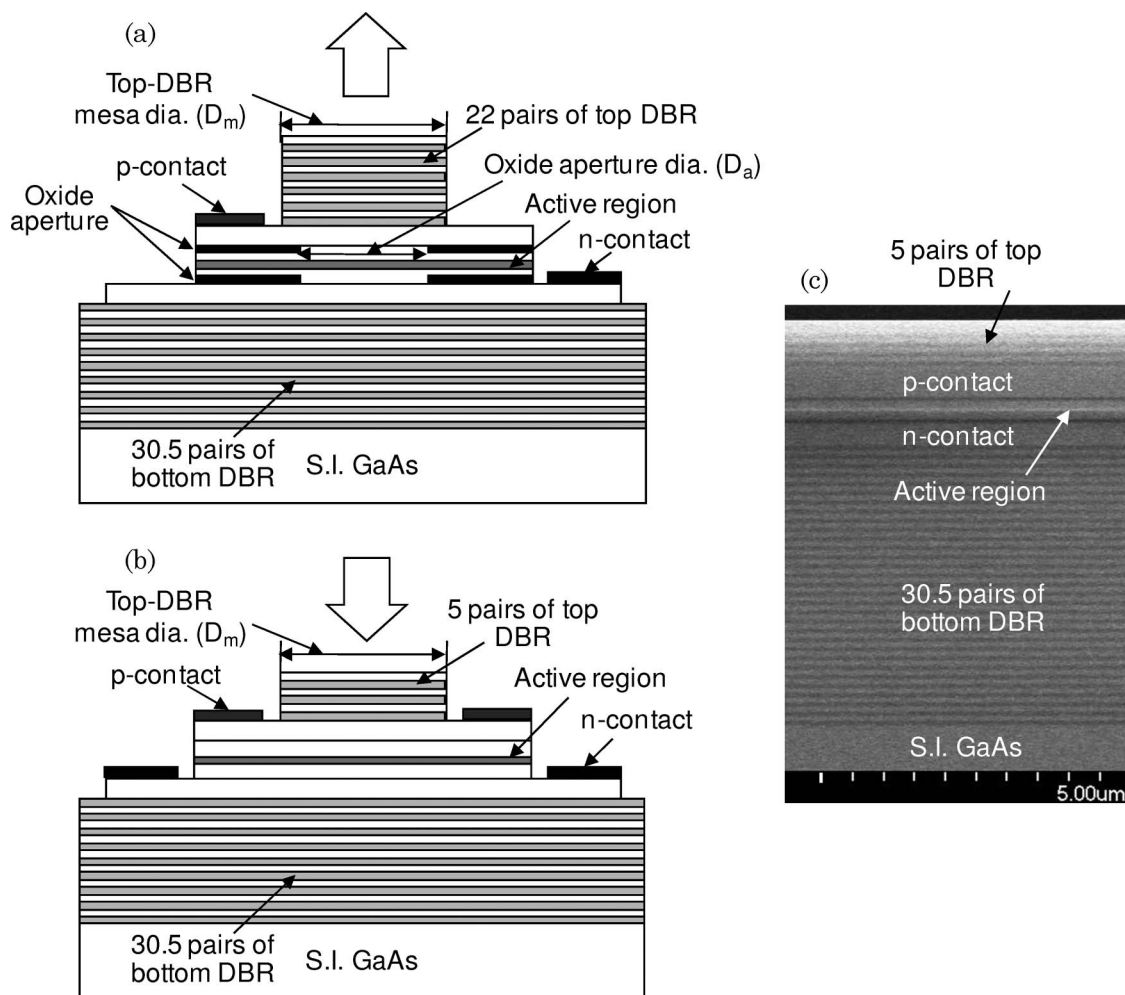


Fig. 1. Schematic illustrations of (a) intracavity-contacted VCSELs with an oxide aperture and (b) intracavity-contacted RCE-PDs from the same epitaxial wafer. A scanning electron microscope image of the grown epitaxial layers is also shown in (c).

and 22 pairs of $\lambda/4$ -thick GaAs/ $\text{Al}_{0.88}\text{Ga}_{0.12}\text{As}$ layers, respectively. In contrast with VCSELs, the RCE-PDs have only 5 pairs of top DBRs without oxide aperture. A scanning electron microscope image of grown epitaxial layers is also shown in Fig. 1(c).

For VCSEL fabrication, the sample was processed into a first cylindrical mesa $18\text{ }\mu\text{m}$ in diameter etched down to the p -GaAs contact layer using an inductively coupled plasma etcher with an *in situ* laser interferometer [15]. Then, the second cylindrical mesa of $54\text{ }\mu\text{m}$ in diameter was etched down to the n -GaAs contact layer. Two $\text{Al}_{0.98}\text{Ga}_{0.02}\text{As}$ layers were selectively oxidized into an oxide aperture diameter (D_a) of $4.5\text{ }\mu\text{m}$ by a wet thermal oxidation process for optical and electrical confinement. The n -contact layer was etched for device isolation, and benzocyclobutene (BCB) was coated on the sample and cured at 210°C for 1 h for passivation and planarization. After exposing the p - and n -GaAs contact layers, Pt/Ti/Pt/Au and Ni/Au/Ge/Ni/Au metals were deposited on the p - and n -GaAs contact layers, respectively, using an electron-beam evaporator. In order to reduce the current crowding at the rim of the oxide aperture, p - and n -contacts were formed asymmetrically to the opposite side. The contacts were alloyed at 425°C for 25 s. For RCE-PD fabrication, the top DBR was etched by removing 17 pairs of GaAs/ $\text{Al}_{0.88}\text{Ga}_{0.12}\text{As}$ layers by inductively coupled plasma etcher. The following fabrication processes were essentially same as those for intracavity-contacted VCSELs except for wet thermal oxidation. The p - and n -contacts were formed symmetrically in the RCE-PD structure. The testing was performed in continuous-wave (CW) mode.

3. Results and Discussion

Figure 2(a) shows the measured reflectance and photoluminescent (PL) spectrum, and 2(b) shows the uniformity of Fabry–Perot (FP) mode wavelength for the grown epitaxial VCSEL layers with 30.5 and 22 pairs of GaAs/ $\text{Al}_{0.88}\text{Ga}_{0.12}\text{As}$ on a 5.08 cm (2 in.) GaAs wafer at room temperature. The structure exhibited a mirror stop band of 93 nm in the wavelength range of 937–1030 nm. The transmission dip (i.e., cavity resonance) near the center of the mirror stop band was 979.8 nm and it corresponds to the FP mode, thus resulting in a VCSEL emission wavelength. For PL measurements, the top DBR was etched to remove the influence of the cavity mode. The peak wavelength of PL emission is about 975 nm, and the full width at half maximum (FWHM) value is about 18 meV, indicating a 7 nm offset from the FP mode. As shown in Fig. 2(b), the average and standard deviation values of the FP mode wavelength measured within a 40 mm diameter were about 982 nm and 0.028 nm, respectively. This corresponds to a wavelength uniformity of 0.003%.

For intracavity-contacted VCSELs with an oxide aperture, the static and dynamic characteristics are affected by the top-DBR mesa diameter as well

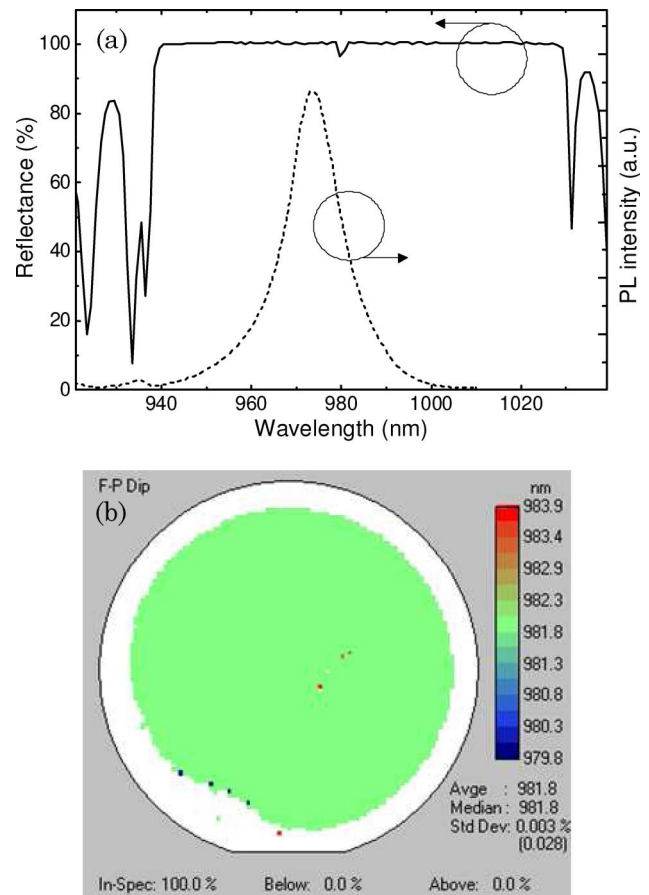


Fig. 2. (Color online) (a) Measured reflectance and PL spectrum and (b) uniformity of the FP mode wavelength for the grown epitaxial VCSEL layers with 30.5 and 22 pairs of GaAs/ $\text{Al}_{0.88}\text{Ga}_{0.12}\text{As}$ on 5.08 cm GaAs wafer at room temperature.

as the oxide aperture diameter. To investigate the influence of mesa size on device performance, VCSELs with top-DBR mesa diameter (D_m) of 12–20 μm by a step of $2\text{ }\mu\text{m}$ were fabricated and characterized. The oxide aperture diameter was fixed to $4.5\text{ }\mu\text{m}$. Figure 3(a) shows the slope efficiency and differential series resistance of the fabricated VCSELs with $D_a = 4.5\text{ }\mu\text{m}$ as a function of top-DBR mesa diameter at 20°C . All the fabricated devices have similar threshold currents of $\sim 1.2\text{ mA}$ because of the same active volume. On the other hand, the maximum output power and differential quantum efficiency are reduced as the top-DBR mesa diameter becomes smaller. The smaller mesa size causes a larger optical loss due to the suppression of the high-order modes in the outer region of top DBR. The mode-selective aperture, formed naturally in the top DBR by wet thermal oxidation, helps the high-order mode suppression [16]. A rapid decrease in the differential quantum efficiency is observed for $D_m < 16\text{ }\mu\text{m}$. This can be explained by the increase of the overlap between the mode-selective aperture and the high-order modes. The differential series resistance of the intracavity-contacted VCSELs is not small compared to the extracavity-contacted VCSELs due to the long lateral conduction length [17]. The smaller

mesa size may lead to a short current path, providing the resultant resistance shrinkage. As shown in Fig. 3(a), the differential series resistance is decreased from 140 Ω to 122 Ω , as the top-DBR mesa diameter is decreased from 20 μm to 12 μm . It is noted that there is a trade-off between the quantum efficiency and the resistance.

The CW light-current-voltage (L-I-V) curves at 20 $^{\circ}\text{C}$ of the 15 fabricated VCSELs with $D_a = 4.5 \mu\text{m}$ and $D_m = 18 \mu\text{m}$ is shown in Fig. 3(b). The insets show the light emission spectrum (on a logarithmic scale) and a microscope image of a fabricated device. The emission wavelength is about 986 nm near threshold. The devices exhibit a threshold current (I_{th}) of ~ 1.19 – 1.32 mA and a slope efficiency of $\eta \sim 0.35$ – 0.37 mW/mA. The differential resistance above I_{th} is approximately 130 Ω . Maximum output power of 3.28–3.49 mW was obtained, and rollover currents were observed around 16 mA. The voltages are ~ 2.6 – 2.7 V at threshold. This means that InGaAs/GaAs VCSEL structures can be grown and fabricated with excellent uniformity over a wide area. As shown in the inset of Fig. 3, the device structure has an asymmetric current injection scheme, which can reduce current crowding effects [14].

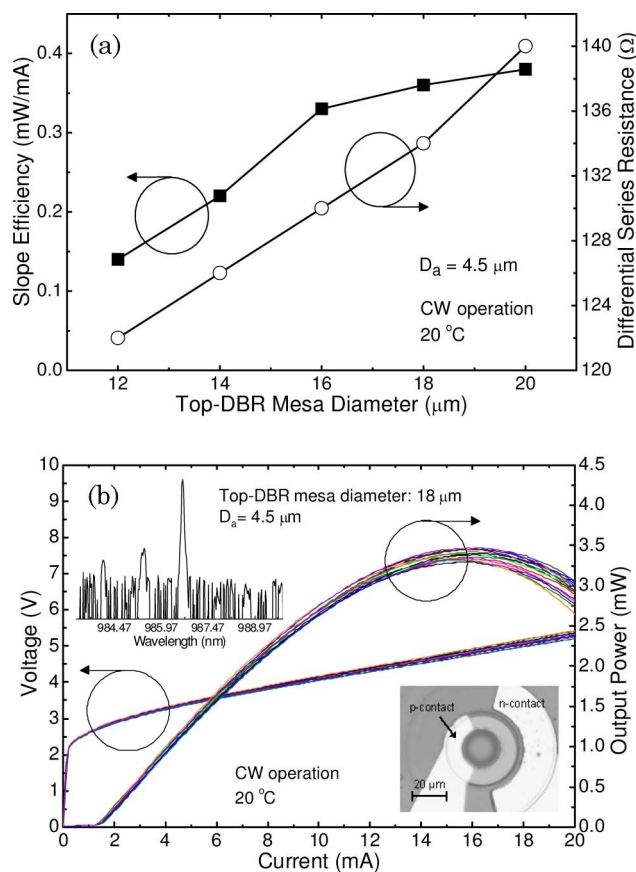


Fig. 3. (Color online) (a) Slope efficiency and differential series resistance of the fabricated VCSELs with $D_a = 4.5 \mu\text{m}$ as a function of top-DBR mesa diameter at 20 $^{\circ}\text{C}$ and (b) CW L-I-V curves at 20 $^{\circ}\text{C}$ of the 15 fabricated VCSELs with $D_a = 4.5 \mu\text{m}$ and $D_m = 18 \mu\text{m}$. The insets show the light emission spectrum and microscope image of a fabricated device.

Figure 4(a) shows the frequency response as a function of frequency of the VCSEL with $D_a = 4.5 \mu\text{m}$ and $D_m = 18 \mu\text{m}$ at $I = 2$ – 7 mA in steps of 1 mA. The operating temperature is 20 $^{\circ}\text{C}$. The small-signal modulation response was measured using a 30 GHz RF spectrum analyzer with a 25 GHz high-speed photodetector. A 40 GHz bias tee was used to combine the DC bias and RF signal from a 20 GHz CW generator. The 3 dB modulation bandwidth was 6.4 GHz at $I = 2$ mA. The modulation bandwidth became larger as the injection current increased. The amount of the overshoot became smaller with injection current. From the measured data, a maximum 3 dB modulation bandwidth of 11.5 GHz was obtained at a bias current of 7 mA. The 3 dB bandwidth as a function of $[I - I_{\text{th}}]^{1/2}$ at 20 $^{\circ}\text{C}$ is shown in Fig. 4(b). The modulation current efficiency factor, i.e., a linear interrelationship between the 3 dB modulation bandwidth and the square root of the driving current above threshold, was obtained

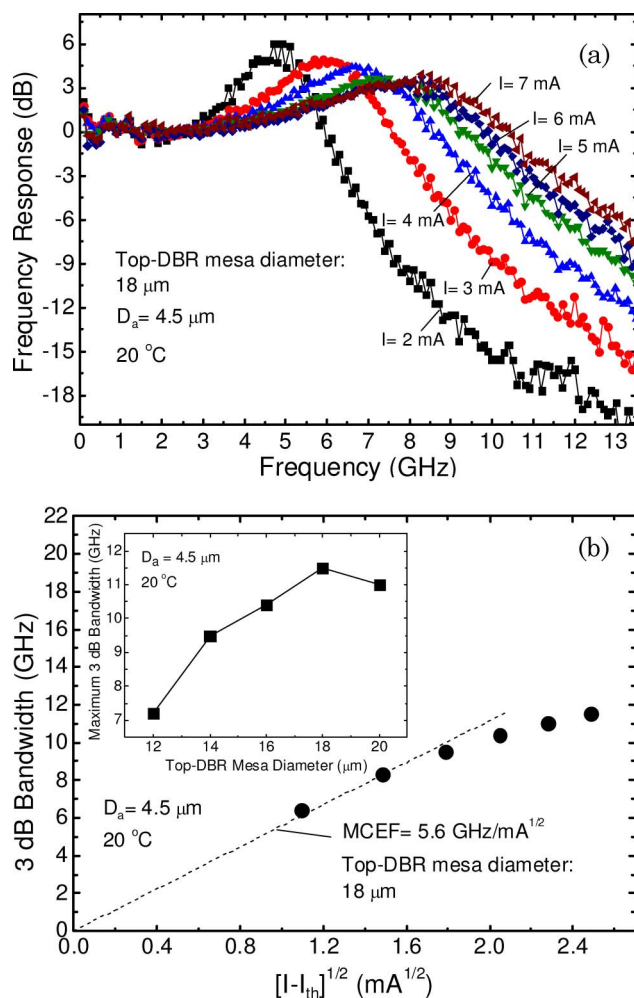


Fig. 4. (Color online) (a) Small signal response as a function of frequency and (b) 3 dB bandwidth as a function of $[I - I_{\text{th}}]^{1/2}$ of the VCSEL with $D_a = 4.5 \mu\text{m}$ and $D_m = 18 \mu\text{m}$ at different injection currents. The inset of (b) shows the maximum 3 dB bandwidth of the fabricated VCSELs with $D_a = 4.5 \mu\text{m}$ versus top-DBR mesa diameter. The operating temperature is 20 $^{\circ}\text{C}$.

from the curve fitting, exhibiting approximately $5.6 \text{ GHz/mA}^{1/2}$. The inset of Fig. 4(b) indicates the maximum 3 dB bandwidth of the VCSELs as a function of top-DBR mesa diameter. The 3 dB bandwidth can be expressed in terms of the output power [18]:

$$f_{3\text{dB}} \cong \frac{1.55}{2\pi} \sqrt{\frac{\lambda v_g a}{hc V_a} \frac{\alpha_i + \alpha_m}{\alpha_m} P_0}, \quad (1)$$

where λ is the emitting wavelength, v_g is the group velocity, a is the differential gain, h is Planck's constant, c is the velocity of light in vacuum, V_a is the effective active volume, α_i is the internal round-trip loss, α_m is the mirror loss, and P_0 is the optical output power. From Eq. (1), the device with higher output power and lower internal loss in the same active volume exhibits a larger bandwidth. On the other hand, the modulation bandwidth can be also determined by the RC time constant related to the device resistance and the parasitic capacitance. For VCSEL structures with $D_a = 4.5 \mu\text{m}$, the 3 dB bandwidth is reduced for small D_m due to the low differential quantum efficiency, while it is also decreased for large D_m due to the high series resistance, leading to an optimum top-DBR mesa diameter of $18 \mu\text{m}$.

For resonant cavity devices with DBR stacks, the optical thickness of the outermost layer of the top DBR is crucial to determine the resonance characteristics [8]. The quantum efficiency, peak wavelength, and spectral bandwidth are changed when the thickness of the outermost layer deviates from an optimum value, i.e., $\lambda/4n$. Figure 5(a) shows the measured and simulated quantum efficiency of symmetric intracavity-contacted RCE-PDs as a function of wavelength for overetched thicknesses of the outermost layer of 15 nm and 50 nm at 20°C . The maximum quantum efficiency is obtained at resonant wavelengths. For RCE-PDs, the top DBRs with 5 pairs of GaAs/Al_{0.88}Ga_{0.12}As were optimized in terms of the quantum efficiency, and the FWHM of spectral response from the simulation. The simulation results are in close agreement with the measurement results. When the top DBR is etched up to 5 pairs from the VCSEL wafer, the extent of the overetching of the outermost layer is very critical. Figure 5(b) shows the measured peak wavelength and maximum quantum efficiency as a function of overetched thickness of outermost layer together with simulated results. The peak wavelength is slightly blueshifted as the overetching proceeds. The quantum efficiency was significantly reduced with further overetching of $>15 \text{ nm}$. After 50 nm overetching, the maximum quantum efficiency was down to 28%. Thus, excessive overetching should be avoided for high device performance. Precise etch-depth control of the top DBR can be achieved by *in situ* laser reflectometry [15].

Figure 6(a) shows the measured responsivity as a function of wavelength under a bias voltage of -5 V at 20°C for the fabricated RCE-PD with $D_m = 18 \mu\text{m}$.

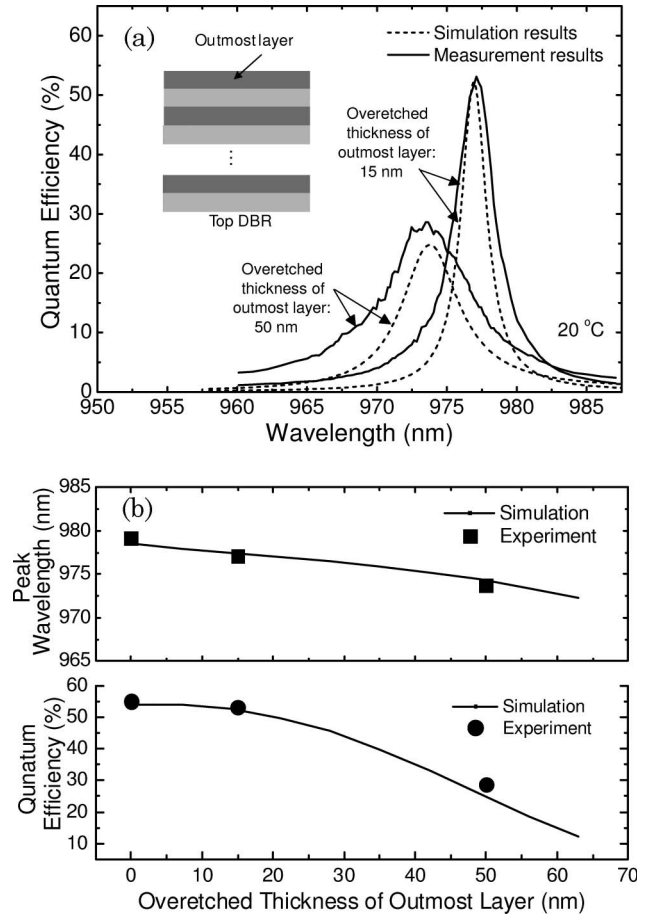


Fig. 5. (a) Measured and simulated quantum efficiency of symmetric intracavity-contacted RCE-PDs as a function of wavelength for the overetched thicknesses of the outermost layers of 15 nm and 50 nm at 20°C and (b) measured peak wavelength and maximum quantum efficiency as a function of overetched thickness of the outermost layer together with simulated results.

The responsivity was measured by an experimental setup that consists of a 980 nm external-cavity tunable laser source, a semiconductor parameter analyzer, an optical spectrum analyzer, and a standard optical powermeter in the dark box. The device exhibited a peak responsivity of 0.44 A/W at a wavelength of 979.7 nm with a spectral width of 3.15 nm . The dark current as a function of reverse bias voltage is shown in the inset of Fig. 6(a). The dark current was increased from 8.78 pA to 2.42 nA as the reverse bias voltage increased from 1 V to 12 V . The dark current was 68 pA at a bias voltage of -5 V , and the reverse breakdown voltage occurred near 13.5 V . As expected, the dark current of the RCE-PD is much less than that of a conventional p-i-n PD. This reduction in dark current may be ascribed mainly to the use of very thin absorption layers [19]. Since the typical photocurrent is of the order of few μA , the ratio of photocurrent to dark current is more than 10^4 .

RCE-PDs have narrow intrinsic absorption regions, leading to high electric fields of $>10 \text{ V}/\mu\text{m}$ in InGaAs/GaAs quantum wells. This results in reduced absorption in quantum wells and degradation

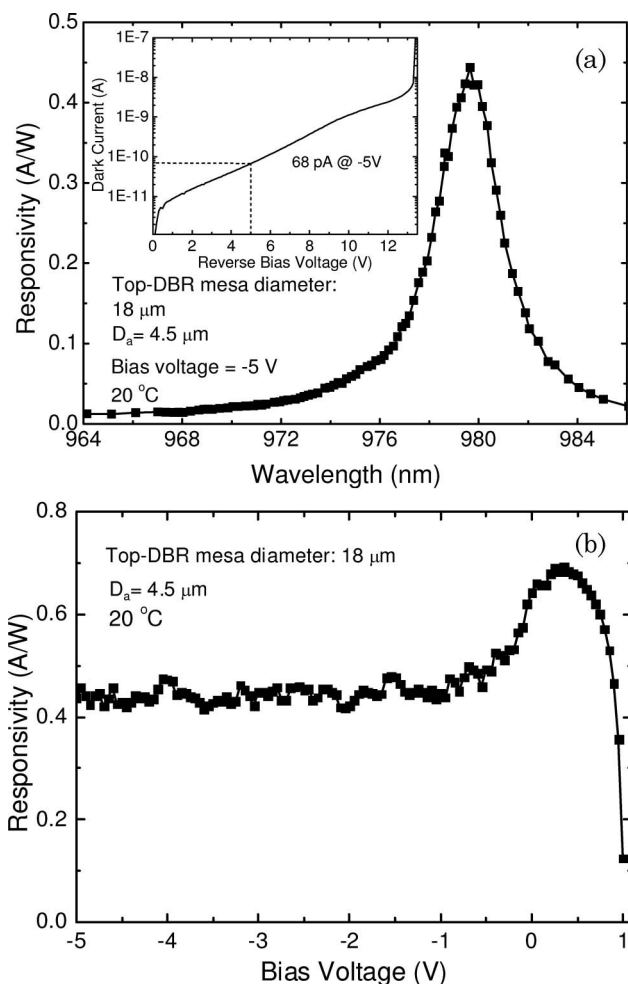


Fig. 6. (a) Measured responsivity as a function of wavelength under a bias voltage of -5 V and (b) measured peak responsivity as a function of bias voltage for the fabricated RCE-PD with $D_m = 18 \mu\text{m}$. The temperature is 20°C . The inset of (a) shows the dark current as a function of reverse bias voltage.

in device performance [20]. The electric field in the quantum wells is reduced by applying a small forward bias to the PD, thus increasing the absorption coefficient. Figure 6(b) shows the measured peak responsivity at 20°C as a function of bias voltage for the fabricated RCE-PD with $D_m = 18 \mu\text{m}$. The peak responsivity reaches a maximum value at a bias voltage of ~ 0.35 V, and then it decreases rapidly with the decrease of bias voltage. With negative bias voltages above 1 V, the peak responsivity remained almost constant since the additional reduction in electric field has minimal effect on the absorption in the quantum wells.

Figure 7 shows the frequency response as a function of frequency under a bias voltage of -5 V at 20°C for a fabricated RCE-PD with a top-DBR mesa diameter of $18 \mu\text{m}$. The inset shows the 3 dB bandwidth as a function of photocurrent. A maximum 3 dB bandwidth of 8.9 GHz was achieved, much larger than that of an extracavity-contacted RCE-PD [12]. The 3 dB bandwidth was reduced as the photocurrent increased. For bias voltage of -5 V and -7 V, the 3 dB

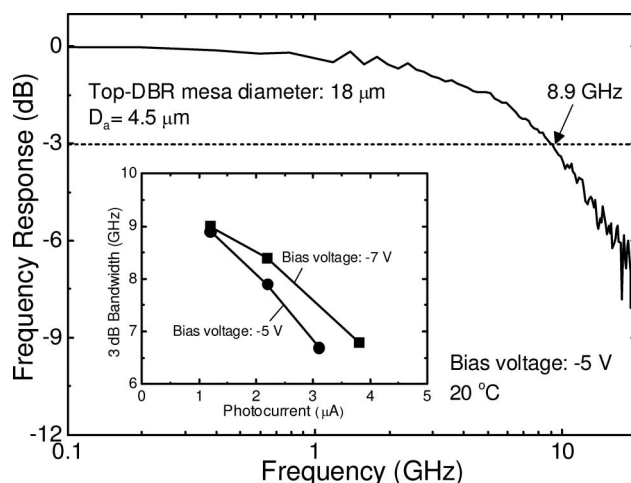


Fig. 7. Frequency response as a function of frequency under a bias voltage of -5 V at 20°C for the fabricated RCE-PD with $D_m = 18 \mu\text{m}$. The inset shows the 3 dB bandwidth as a function of photocurrent at bias voltage of -5 V and -7 V.

bandwidth was 8.9 GHz and 9 GHz, respectively, at a photocurrent of $1.2 \mu\text{A}$. A 3 dB bandwidth of 6.7 GHz at -5 V was observed at the photocurrent of $3.1 \mu\text{A}$. At a bias voltage of -7 V, the 3 dB bandwidth is 6.8 GHz at a photocurrent of $3.8 \mu\text{A}$. Therefore, in order to fully utilize the available maximum bandwidth for optical interconnects, the output power of VCSELs and the relative alignment position of waveguides and RCE-PDs should be appropriately chosen to keep the photocurrent as low as a specified value for the desired 3 dB bandwidth.

4. Conclusions

We demonstrated the high-speed characteristics of 980 nm InGaAs/GaAs VCSELs and RCE-PDs based on intracavity-contacted structure from the same epitaxial wafer, indicating excellent uniformity over a wide area. Twenty-two and 5 pairs of top DBRs were employed for VCSELs and RCE-PDs, respectively. The fabricated VCSEL with $D_a = 4.5 \mu\text{m}$ and $D_m = 18 \mu\text{m}$ emitted a maximum output power of 3.49 mW with a maximum 3 dB bandwidth of 11.5 GHz and a modulation current efficiency factor of $5.6 \text{ GHz}/\text{mA}^{1/2}$. For RCE-PDs based on VCSEL structure, a peak responsivity of 0.44 A/W at 979.7 nm with a spectral width of 3.15 nm was obtained. The PD operated up to a 3 dB bandwidth of 9 GHz. These results provide a great potential to monolithically integrate VCSELs and RCE-PDs on the same substrate for high-speed optical interconnects with 10 GHz modulation bandwidth.

This work was supported by Gwangju Institute of Science and Technology Top Brand Project “Photonics 2020,” Korea.

References

1. D. A. B. Miller, “Rationale and challenges for optical interconnects to electronic chips,” *Proc. IEEE* **88**, 728–749 (2000).
2. A. F. Benner, M. Ignatowski, J. A. Kash, D. M. Kuchta, and M. B. Ritter, “Exploitation of optical interconnects in future

- server architectures," IBM J. Res. Develop. **49**, 755–776 (2005).
3. E. Mohammed, A. Alduino, T. Thomas, H. Braunsch, D. Lu, J. Heck, A. Liu, I. Young, B. Barnett, G. Vandentop, and R. Mooney, "Optical interconnect system integration for ultra-short-reach applications," Intel Technol. J. **8**, 115–128 (2004).
4. B. Jalali and S. Fathpour, "Silicon photonics," J. Lightwave Technol. **24**, 4600–4615 (2006).
5. N. Izhaky, M. T. Morse, S. Koehl, O. Cohen, D. Rubin, A. Barkai, G. Sarid, R. Cohen, and M. J. Paniccia, "Development of CMOS-compatible integrated silicon photonics devices," IEEE J. Sel. Topics Quantum Electron. **12**, 1688–1698 (2006).
6. D. M. Kuchta, Y. H. Kwark, C. Schuster, C. Baks, C. Haymes, J. Schaub, P. Pepeljugoski, L. Shan, R. John, D. Kucharski, D. Rogers, M. Ritters, J. Jewell, L. A. Graham, K. Schrödinger, A. Schild, and H. Rein, "120 Gb/s VCSEL-based parallel-optical interconnect and custom 120 Gb/s testing station," J. Lightwave Technol. **22**, 2200–2212 (2004).
7. R. Szweda, "VCSEL applications diversify as technology matures," III-V Rev. **19**, 34–38 (2006).
8. I. Chung and Y. T. Lee, "A method to tune the cavity-mode wavelength of resonant cavity-enhanced photodetectors for bi-directional optical interconnects," IEEE Photon. Technol. Lett. **18**, 46–48 (2006).
9. A. C. Alduino, S. Q. Luong, Y. Zhou, C. P. Hains, and J. Cheng, "Quasi-planar monolithic integration of high-speed VCSEL and resonant enhanced photodetector arrays," IEEE Photon. Technol. Lett. **11**, 512–514 (1999).
10. Y. Zhou, J. Cheng, and A. A. Allerman, "High-speed wavelength-division multiplexing and demultiplexing using monolithic quasiplanar VCSEL and resonant photodetector array with strained InGaAs quantum wells," IEEE Photon. Technol. Lett. **12**, 122–124 (2000).
11. D. A. Loudereback, O. Sjölund, E. R. Hegblom, S. Nakagawa, J. Ko, and L. A. Coldren, "Modulation and free-space link characteristics of monolithically integrated vertical-cavity lasers and photodetectors with microlenses," IEEE J. Sel. Topics Quantum Electron. **5**, 157–165 (1999).
12. T. Knodel, H. K. H. Choy, J. L. Pan, R. King, R. Jäger, G. Lullo, J. F. Ahadian, R. J. Ram, C. G. Fonstad Jr., and K. J. Ebeling, "RCE photodetectors based on VCSEL structure," IEEE Photon. Technol. Lett. **11**, 1289–1291 (1999).
13. J. W. Scott, B. J. Thibeault, D. B. Young, L. A. Coldren, and F. H. Peters, "High efficiency submilliamp vertical cavity lasers with intracavity contacts," IEEE Photon. Technol. Lett. **6**, 678–680 (1994).
14. A. V. Krishnamoorthy, L. M. F. Chirovsky, W. S. Hobson, J. Lopata, J. Shin, R. Rozier, and J. E. Cunningham, "Small-signal characteristics of bottom-emitting intracavity contacted VCSEL's," IEEE Photon. Technol. Lett. **12**, 609–611 (2000).
15. Y. M. Song, K. S. Chang, B. H. Na, J. S. Yu, and Y. T. Lee, "Precise etch-depth control of microlens-integrated intracavity-contacted vertical-cavity surface-emitting lasers by in situ laser reflectometry and reflectivity modeling," Thin Solid Films doi: 10.1016/j.tsf.2009.03.198 (accepted 25 March 2009, in press).
16. K. S. Chang, Y. M. Song, and Y. T. Lee, "Stable single-mode operation of VCSELs with a mode selective aperture," Appl. Phys. B **89**, 231–234 (2007).
17. Y. M. Song, K. S. Chang, B. H. Na, J. S. Yu, and Y. T. Lee, "Low thermal resistance, high-speed 980 nm asymmetric intracavity-contacted oxide-aperture VCSELs," Phys. Status Solidi A doi: 10.1002/pssa.200824458 (published online 22 April 2009).
18. L. A. Coldren and S. W. Corzine, *Diode Lasers and Photonic Integrated Circuits* (Wiley, 1995).
19. M. Gokkavas, O. Dosunmu, M. S. Uulu, G. Ulu, R. P. Mirin, D. H. Christensen, and E. Ozbay, "High-speed high-efficiency large-area resonant cavity enhanced p-i-n photodiodes for multimode fiber communications," IEEE Photon. Technol. Lett. **13**, 1349–1351 (2001).
20. M. Ghisoni, O. Sjölund, A. Larsson, S. M. Wang, J. Thordsson, T. G. Andersson, and L. Hart, "A comparative study of strain relaxation effects on the performance of InGaAs quantum well based on heterojunction phototransistors," IEEE J. Sel. Top. Quantum Electron. **3**, 768–779 (1997).